

CHARACTERIZATION OF SURFACE FEATURES GENERATED BY SPACE WEATHERING ON LUNAR AND ASTEROIDAL REGOLITH GRAINS. J. J. Gillis-Davis¹, K. K. Ohtaki², R. C. Ogliore¹, H. A. Ishii², and J. P. Bradley², ¹Washington University in St. Louis, Department of Physics, One Brookings Dr., St. Louis, MO, 63130, ²Hawai'i Institute of Geophysics and Planetology, 1680 East-West Road, University of Hawai'i at Mānoa, Honolulu, HI 96822, USA (j.gillis-davis@wustl.edu).

Introduction: Mercury, the Moon, and asteroids undergo spectral, compositional, and physical changes to their surface materials as a result of exposure to the space environment [1-9]. While the surfaces of these airless bodies display some similar indicators of space weathering, each body has its own particular set of space-weathering effects [7]. Differences in spectral response likely arise from diversities in target composition/grain size, solar distance, local environmental factors, and length of exposure to space [7-11].

Hence, we turn to micro-analyses of lunar and asteroidal regolith grains in order to understand space weathering at the nm-scale dimensions over which it takes place. We compare and contrast textures and chemical compositions of features at/near the surface of these grains with the aim of linking particular surface features with a specific space weathering process. Although previous studies find that features formed by micrometeorites are rare on the surfaces of regolith grains from Itokawa, they are present [12,13], but even the relative abundance of features on grains from different planetary bodies can be informative.

Samples & Methods: We studied grains from an Apollo 11 regolith sample 10084, which consists of the <1 mm sieve-size fraction. Approximately 100 grains were placed on carbon tape mounted on an aluminum SEM stub. Backscatter electron (BSE) and secondary electron (SE) images were acquired for nearly all grains and used to select features for Focused Ion Beam (FIB) sectioning and TEM analyses.

The Tescan MIRA3 field emission scanning electron microscope at Washington University in St. Louis was used to obtain BSE and SE images. SE images were acquired at 2.0 kV. Physical features on the surface were identified with SE images, while Z-contrast SE images helped identify nanophase iron metal (npFe) in the upper surfaces of grains.

Electron transparent samples were prepared using the FEI Helios NanoLab 660 DualBeam FIB instrument at the University of Hawaii Advanced Electron Microscopy Center. To examine micro-textures, -petrography, and -chemistry of the space-weathered grains, an FEI 80–300 kV Titan, dual Cs-corrected, monochromated (scanning) transmission electron microscope, or (S)TEM was used. Brightfield (BF), high-angle annular dark field (HAADF), diffraction patterns, and chemical analysis via energy dispersive X-ray elemental (EDS) were acquired for each FIB section. EDS maps were acquired on an FEI TitanX 60–300 (S)TEM (Molecular Foundry, Berkeley, CA).

Results & Discussion: The following surface features were observed in SE and BSE images: three types of pits, discoid or circular/ellipsoidal melt deposits (CEMD), two types of splash melt, adhered particles, blistering, iron metal blebs, conchoidal fracturing, abrasion/impression features, and microcraters (aka zap pits). Due to space restrictions, we only describe pits and CEMDs in this abstract.

Pits are small holes of non-impact origin and are categorized in three main types. The distinguishing features of *Type I* pits are: found exclusively on agglutinitic glass and splash melt, exhibit no floor, generally have raised and/ thickened rims, and circumferences are circular to elliptical (Fig. 1). The diameter of these pits ranges from 0.1 to 1 μm . Cross sections into surfaces containing these pits reveal vesicular internal texture of the glass. On the basis of these characteristics, we suggest these pits formed as the result of volatile release — with gas escaping from the glass or from the substrate on which the hot melt landed. Bubbles intersected the melt surface. The viscosity of the melt was too high for the hole to close. The thickened rim formed when the bubble ruptured and the edges viscoelastically rebounded back onto the surface. These pits are abundant on lunar agglutinitic glass and found in a melt splash on an Itokawa grain by [14]. These pits might be mistaken for impact craters in low-magnification SE images because of their raised rims [15].

Type II pits are found on impact melt beads that are associated with micro-impact craters [16]. The pits are found approximately antipodal to the crater and along the portion of the crater rim. The bowl shaped, rimless pits are circular with a uniform diameter that averages $\sim 2 \mu\text{m}$ (Fig. 2a). The pits appear generated by shock and heating related to the micrometeorite impact event. This formation mechanism was suggested for pits formed in ion and laser irradiation experiments [17].

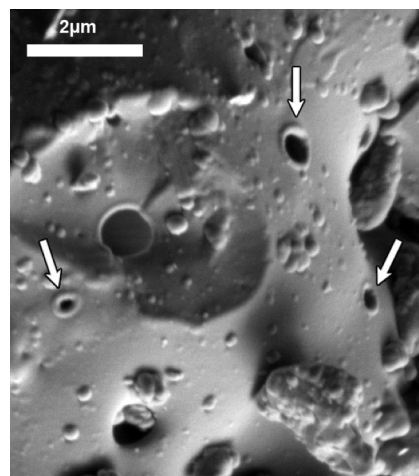


Fig 1. SE image of pits with raised rims, which are formed in agglutinitic glass.

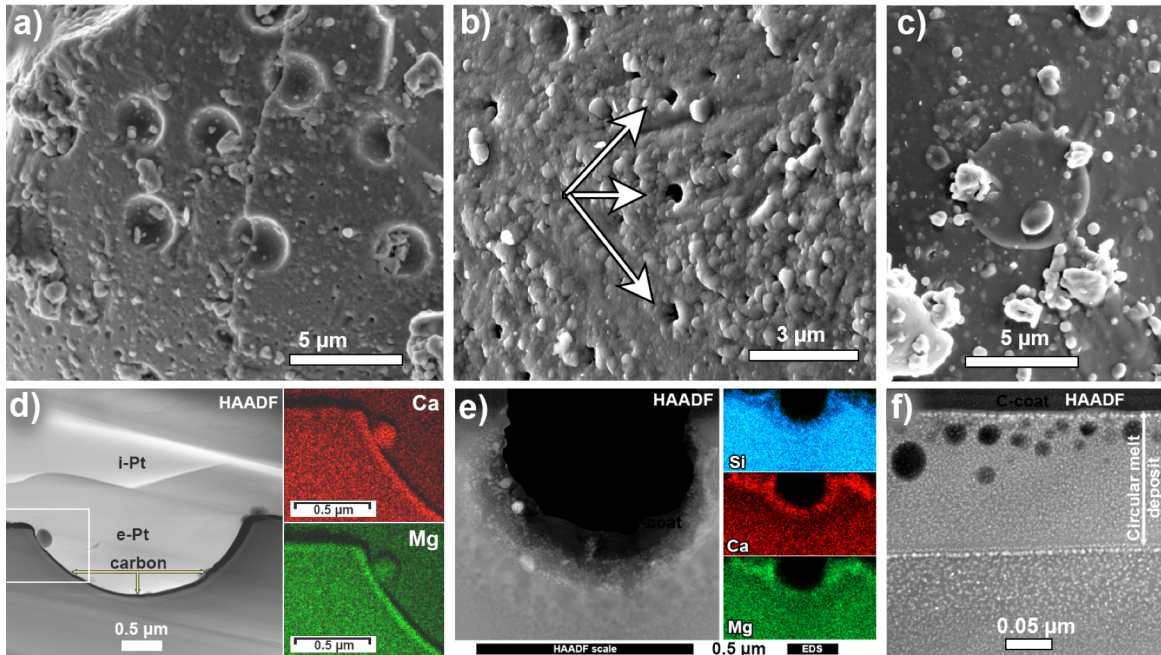


Fig. 2 SEM SE images (a,b,c) of surface features on lunar grains: a) large bowl-shaped pits antipodal to zap pit with small irregular pits in the interstices between large pits, b) small irregular pits (arrows), and c) discoid melt. STEM data of features in a–c: d) HAADF image of bowl-shaped pit. Box depicts location of EDS composition data, which shows Ca and Mg are enriched in pit wall relative to surface outside the pit. Coatings of carbon, and electron- (e-Pt) and ion- (i-Pt) deposited platinum are placed down as part of the FIB process. e) HAADF image of small irregular pit. The substructure of the pit floor appears granular. EDS images show Ca and Mg are enriched inside and outside the pit while Si is depleted in both locations. f) HAADF image reveals vesicles in the upper half of CEMD (dark circles). npFe (bright circles) is evenly dispersed throughout the CEMD and host grain under it. The CEMD-grain interface and surface of the CEMD show a concentrated layer of npFe.

Type III pits occur on glassy grain surfaces — both impact melt glass and amorphous rims. These pits are the smallest of all three pit types with average size of $\sim 0.5 \mu\text{m}$ (Fig. 2b). Another difference from the previous two pit types is that the rims of these pits are not sharp. We infer that these pits were once sharp and smooth morphology but the form has degraded with weathering.

Circular/ellipsoidal melt deposits are raised circular features found on many grain surfaces (Fig. 2c). They are a common feature on lunar grains [18] but found infrequently on asteroid grains [14]. CEMDs exhibit a pancake-like width-to-height aspect ratio. For lunar grains, this aspect ratio is approximately 30:1, and the ratio still needs to be measured for asteroidal grains. The diameter of these melt deposits on lunar samples ranges from $0.3 \mu\text{m}$ to $6 \mu\text{m}$. On the basis of EDS mapping of one CEMD, we can confirm that these melt deposits are not part of the original grain but splashes of molten material [13,17]. The CEMD contains 33% less Si, double the amount of Ti, and 50% more Ca and Mg relative to the grain that it is superposed on.

Conclusions: All of the pits presented here (Figs 1 and 2a,b) suggest volatile loss from the regolith. Impact heating is the proposed catalyst for volatile release in Type I and II pits. Further study of Type III pits is needed to determine their origin. CEMDs looked analogous

to popped vesicle lids reported by [17], however, EDS compositional mapping indicates the discoid features are accretionary objects as suggested by [14,18]. These findings signify that classifying grain morphologies into categories, measuring their composition, and comparing with the material on which the features formed, may serve to untangle different modes of weathering that act on a body and their relative proportions.

References: [1] Keller, L. P. and McKay, D. S., 1997. *GCA*, **61**, 2331; [2] Pieters, C.M. et al., 2000, *MAPS*, **35**, 1101; [3] Hapke, B. 2001, *JGR*, **106**, 10039; [4] Noble, S. K., & Pieters, C. M., 2003. *Solar System Research*, **37**(1), 31; [5] Chapman, C. 2004, *Annu. Rev. Earth Planet. Sci.*, **32**, 539; [6] Gaffey, M. J., 2010. *Icarus*. **209**, 564-574; [7] Pieters, C. M., Noble, S. K., 2016. *JGR: Planets*. **121**, 1865; [8] Domingue, D. L. et al., 2014. *Space Sci. Rev.*, **181**(1-4), 121; [9] Brunetto, R., et al., 2015. *Asteroids IV*. Univ. of Arizona, Tucson, 597; [10] Kaluna, H. M., et al., 2017, *Icarus*, **292**, 245; [11] Corley, L.M. et al., 2016. *LPSC 47*, Abstract #2692; [12] Nakamura, E., et al., 2016. *PNAS* **109**, E624; [13] Matsumoto, T., et al., 2018. *Icarus* **303**, 22-33. [14] Dobrică, E., Ogliore, R., 2016. *Earth, Planets and Space* **68**, 21; [15] Schneider, E., et al., 1975. *4th LPSC*, 3277; [16] Gillis-Davis et al., 2019, EPSC Abstracts Vol. 13, EPSC-DPS2019-61-2; [17] Zhu, C., et al., 2019. *PNAS*, **116**, 23, 11165; [18] Morrison, D. A., et al., 1976. *4th LPSC*, 3235.